RESEARCH ARTICLE

Key Points:
- Observational evidence of slope-induced straining could be reproduced with a one-dimensional numerical model
- Earth rotation induces a significant along-slope flux of suspended sediment
- When the main current is orientated along-slope, the tidal pumping contribution to the cross-slope flux is reduced or inverted

Correspondence to:
K. Schulz,
kirstin.schulz@nioz.nl

Slope-induced tidal straining: Analysis of rotational effects

Kirstin Schulz[1] [ID], Takahiro Endoh[2], and Lars Umlauf[1] [ID]

[1]Leibniz-Institute for Baltic Sea Research Warnemünde, Warnemünde, Germany, [2]UTokyo Ocean Alliance, University of Tokyo, Tokyo, Japan

Abstract Tidal straining is known to be an important factor for the generation of residual currents and transports of suspended matter in the coastal ocean. Recent modeling studies and field experiments have revealed a new type of "slope-induced" tidal straining, in which the horizontal density gradient required for this process is induced by the presence of a slope rather than by river runoff (as in classical tidal straining). Slope-induced tidal straining is investigated here with the help of an idealized numerical model, and results are compared to a recent data set from the East China Sea providing first direct observational evidence. The focus of this study is on the effect of rotation that was ignored in previous investigations. The model is shown to reproduce the key features of the observations, in particular the strain-induced generation of unstable stratification in the bottom boundary layer during periods of upslope flow. Rotation effects are found to significantly reduce the upslope tidal pumping of suspended material and also give rise to a newly identified pumping mechanism that results in a vigorous transport of suspended material along the slope. It is shown that slope-induced tidal straining is likely to be relevant for a wide range of oceanic slopes exposed to tidal motions.
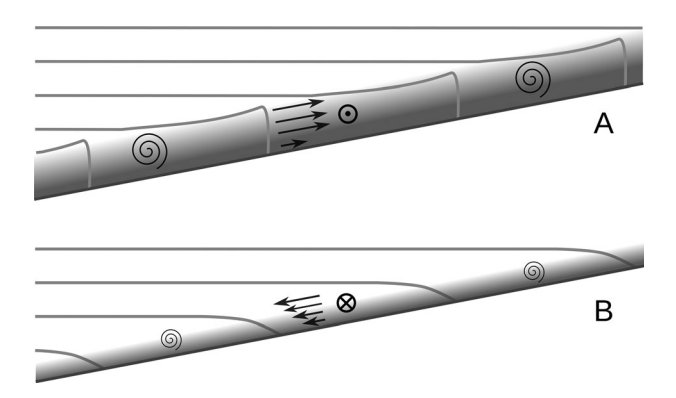
1. Introduction

In many estuaries and regions of the coastal ocean, the tidal dynamics and the generation of residual transports are strongly modified by the presence of a horizontal density gradient, typically maintained by river runoff, differential heating, and horizontal variations in mixing. In these cases, the horizontal density gradient interacts with the vertical tidal shear to induce a periodic modulation of the vertical density structure that is usually referred to as Strain-Induced Periodic Stratification (SIPS). During flood, dense water is advected on top of lighter water, thus destabilizing the water column, whereas during ebb, light water is transported on top of denser water, inducing stable stratification [*van Aken*, 1986; *Simpson et al.*, 1990].

MacCready and Geyer [2014] summarized the present understanding of the dynamical implications of this tidal straining process, highlighting in particular the role of SIPS for the generation of tidal asymmetries in mixing (see their Figure 2). They pointed out that the generally larger turbulent diffusivities observed in estuaries during the less stratified flood phase are reflected in tidal asymmetries in the velocity profiles, inducing a landward residual circulation near the bottom, and a seaward return current in the upper part of the water column. From extensive numerical experiments, *Burchard and Hetland* [2010] concluded that in tidally energetic systems the contribution of this "tidal straining circulation" to the total residual circulation may be significantly larger than the gravitationally driven component, challenging the classical view of estuarine circulation.

Jay and Musiak [1994] proposed that the mixing asymmetries due to SIPS may also have a profound impact on the residual transport of suspended material. These authors showed that due to stronger turbulence during the flood phase, high concentrations of suspended material are generally correlated with flood currents (directed landward), thus inducing a residual landward transport of suspended material [*Uncles et al.*, 1985; *Jay and Musiak*, 1994; *Scully and Friedrichs*, 2007]. Idealized numerical experiments revealed that this "tidal pumping" mechanism generally dominates over the advection of suspended material by the residual current [*Burchard et al.*, 2013].

In a recent modeling study, *Schulz and Umlauf* [2016] proposed that similar tidal straining and pumping processes may occur also in vicinity of a topographic slope—with the important difference, however, that no

Figure 1. Slope-induced tidal straining causing (a) unstable stratification during upslope flow and (b) stable stratification during downslope flow (SIPS). Gray lines denote isopycnals, arrows show the current direction. Gray-shaded areas near the bottom indicate the presence of suspended material; spirals symbolize near-bottom turbulence.

externally imposed horizontal density gradient (e.g., due to river runoff) is required. In this case, the vertical interior density gradient includes a cross-slope (cross-isobath) component that is a function of the slope angle (Figure 1). As the slope angle α is typically small ($\alpha \ll 1$), the cross-slope density gradient is nearly horizontal, and therefore plays a dynamical role comparable to that of the horizontal density gradient in classical tidal straining.

Slope-induced tidal straining is confined to a turbulent bottom boundary layer (BBL), but the process is otherwise completely analogous to classical tidal straining over a flat bottom: during upslope flow, dense water is advected on top of lighter water, resulting in unstable stratification, enhanced near-bottom turbulence, and high concentrations of suspended material (Figure 1a). Vice versa, during downslope flow, the straining of the cross-slope density gradient induces a tendency for increasing stratification inside the BBL, which in turn leads to reduced BBL turbulence, smaller BBL thicknesses, and lower sediment concentrations. Using an idealized one-dimensional (slope-normal) numerical model, *Schulz and Umlauf* [2016] showed that tidal pumping leads to a net cross-slope transport of suspended material, similar to the tidal pumping mechanism over a flat bottom described by *Jay and Musiak* [1994]. In their study, *Schulz and Umlauf* [2016] ignored the effect of rotation, which may, however, be essential in many realistic settings. This point will therefore be investigated in detail in the following analysis.
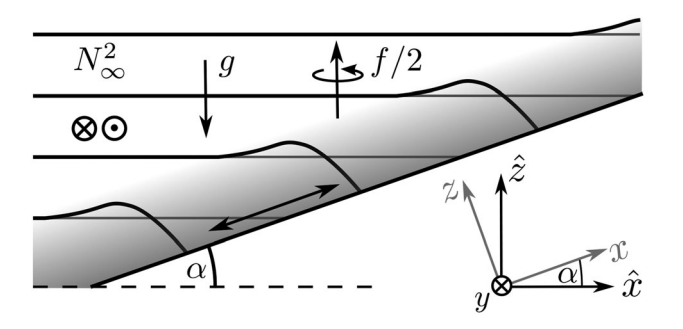
First observational evidence for slope-induced tidal straining was recently discussed by *Endoh et al.* [2016], who analyzed an extensive data set, including turbulence microstructure observations, from a topographic slope exposed to strong tidal currents in the East China Sea. These authors described a periodic destabilization of the water column during periods with upslope tidal currents, induced by the presence of a persistent cross-slope density gradient. The latter turned out to be consistent with the projection of the vertical density gradient onto the cross-slope direction, and therefore with the importance of slope-induced tidal straining.

Here we attempt to clarify the mechanisms, implications, and relevance of slope-induced tidal straining on a real oceanic shelf by combining the results from previous modeling studies by *Umlauf and Burchard* [2011] and *Schulz and Umlauf* [2016] with the experimental data by *Endoh et al.* [2016]. In section 2, we extend the model used by *Schulz and Umlauf* [2016] to include the effects of rotation before we briefly summarize the field observations discussed by *Endoh et al.* [2016] in section 3. After deriving model parameters from these observations in section 4, we present the model results in section 5, and compare them to the field data. The implications of tidal straining for the generation of residual currents and the residual transport of suspended material are analyzed in section 6 before we provide a short discussion of our results and draw some conclusions in section 7.

2. Model Description

2.1. Model Geometry

Following previous modeling studies of slope-induced straining [*Umlauf and Burchard*, 2011; *Schulz and Umlauf*, 2016], we investigate in the following the motion of a vertically stratified Boussinesq fluid in the vicinity of a uniform slope with slope angle α. The geometry is two-dimensional with the horizontal and vertical coordinates denoted by $\hat{x}$ and $\hat{z}$, respectively, and the fluid is assumed to rotate with angular velocity $f/2$ about the vertical axes (Figure 2). Vertical stratification is quantified with the help of the buoyancy frequency,

Figure 2. Schematic view of the model geometry and density structure (black lines) near a uniform slope with slope angle α. Gray lines indicate isopycnal equilibrium levels ($b_\infty = const.$). The cross-slope, along-slope, and slope-normal coordinates are denoted by x, y, and z, respectively. f denotes the Coriolis frequency, N_∞^2 the constant buoyancy frequency (squared) in the interior region, and g the acceleration of gravity. The double arrows symbolize the oscillating near-bottom currents.

$$N^2 = \frac{\partial b}{\partial \hat{z}} , \tag{1}$$

where b denotes buoyancy. Above the BBL, we assume that isopycnals remain strictly horizontal during all times and that N^2 approaches the constant background value N_∞^2. Close to the bottom, however, isopycnals will be distorted as a result of boundary mixing, and the local buoyancy b will differ from the equilibrium buoyancy b_∞ (black and gray lines in Figure 2).

Introducing a rotated coordinate system with the cross-slope, along-slope, and slope-normal coordinates denoted by x, y, and z (see Figure 2), it can be shown from simple geometrical arguments that under the above conditions also the cross-slope buoyancy gradient is constant

$$\frac{\partial b}{\partial x} = N_\infty^2 \sin \alpha , \tag{2}$$

illustrating the generation of a quasi-horizontal ($\alpha \ll 1$) buoyancy gradient by the projection of the purely vertical interior stratification onto the slope [*Garrett et al.*, 1993; *Umlauf and Burchard*, 2011].

2.2. Model Equations

Assuming that all cross-slope and along-slope gradients vanish, except the cross-slope buoyancy gradient defined in (2), the problem becomes geometrically one-dimensional in the slope-normal z-direction. The Boussinesq equations can then be written as [*Umlauf et al.*, 2015]

$$\frac{\partial u}{\partial t} - fv \cos \alpha = (b - b_\infty) \sin \alpha + P_x - \frac{\partial \tau_x}{\partial z} , \tag{3}$$

$$\frac{\partial v}{\partial t} + fu \cos \alpha = P_y - \frac{\partial \tau_y}{\partial z} , \tag{4}$$

$$\frac{\partial b}{\partial t} = -u N_\infty^2 \sin \alpha - \frac{\partial G}{\partial z} , \tag{5}$$

with u and v denoting the cross-slope (positive meaning upslope) and along-slope velocities, τ_x and τ_y the slope-normal turbulent fluxes of momentum, and G the slope-normal turbulent buoyancy flux (all turbulent fluxes are defined per unit mass). $P_x(t)$ and $P_y(t)$ are integration constants that play the role of prescribed external pressure gradients. The cross-slope buoyancy gradient in the advection term in (5) has been expressed with the help of (2). Note that in contrast to previous studies of slope-induced tidal straining that only considered the plane nonrotating case ($f = 0$, $v = 0$), equations (3–5) now include rotational effects that turned out to be essential to describe the motions at our study site.

The equilibrium buoyancy b_∞ appearing in the first term on the right-hand side of (3) evolves as a result of cross-slope buoyancy advection and can therefore be described by an advection equation of the form,

$$\frac{\partial b_\infty}{\partial t} + u_\infty N_\infty^2 \sin \alpha = 0 , \tag{6}$$

which directly follows from (5) for $z \to \infty$.

Far away from the boundary ($z \to \infty$), we assume that all slope-normal gradients, except the buoyancy gradient, vanish, whereas at the lower boundary ($z = 0$) we use the boundary conditions

$$u=v=0, \quad \frac{\partial b}{\partial z}=0 \,. \tag{7}$$

Schulz and Umlauf [2016] also discussed a simple transport equation for the concentration c of suspended particulate material (SPM) exhibiting a vertical sinking motion w_s relative to the moving fluid

$$\frac{\partial c}{\partial t}=-\frac{\partial}{\partial z}(F_z-cw_s\cos\alpha)\,, \tag{8}$$

where F_z is the slope-normal turbulent SPM flux. At the bottom, this flux equals the erosion flux

$$F_z=\alpha_e\max\left\{\frac{|\tau_b|}{\tau_c}-1,0\right\} \quad \text{at } z=0\,, \tag{9}$$

where α_e is the erosion parameter, τ_b the bottom stress, and τ_c the critical shear stress for erosion.

The turbulent fluxes appearing in (3)–(5) and (8) are computed from gradient expressions of the form

$$\tau_x=-v_t\frac{\partial u}{\partial z}\,, \quad \tau_y=-v_t\frac{\partial v}{\partial z}\,, \quad G=-v_t^b\frac{\partial b}{\partial z}\,, \quad F_z=-v_t^b\frac{\partial c}{\partial z}\,, \tag{10}$$

where v_t is the turbulent viscosity and v_t^b is the turbulent diffusivity of buoyancy and SPM. The diffusivities are computed from a second-moment turbulence model that includes two prognostic equations for the turbulent kinetic energy k and the dissipation rate ε. This turbulence model is identical to that described in detail in *Umlauf and Burchard* [2011], *Umlauf et al.* [2015], and *Schulz and Umlauf* [2016], and, for brevity, this description is not repeated here. The general properties of this class of turbulence models are reviewed in *Umlauf and Burchard* [2005]; details about the numerical implementation may be found in *Umlauf et al.* [2005]. In the nonturbulent region above the BBL ($z \to \infty$), the turbulent fluxes are assumed to vanish. Also, as we only investigate flows at high Reynolds number in this study, all molecular fluxes are ignored.

2.3. Model Properties

In the following, we will assume that BBL motions are driven by a harmonic horizontal pressure force pointing into an arbitrary horizontal direction, here referred to as the n direction

$$P_n=P\cos(\omega t+\phi)\,, \tag{11}$$

where ω is the forcing frequency, ϕ the phase, and P the magnitude of the pressure force. Denoting the angle between the n and x directions as β, the components of P_n in the x and y directions are $P_x=P_n\cos\beta$ and $P_y=P_n\sin\beta$. It is straightforward to show from (3) and (4) that for the harmonic forcing in (11), the velocities in the inviscid region above the BBL ($z \to \infty$) are described by

$$u_n=P\frac{\omega}{\omega^2-f^2}\sin(\omega t+\phi), \tag{12}$$

$$u_s=P\frac{f}{\omega^2-f^2}\cos(\omega t+\phi)\,, \tag{13}$$

with u_n and u_s denoting the components in the n and s directions, respectively (the latter obtained from rotating the y axis by the angle β). For $\omega > f$, the velocity vector is seen to anticyclonically trace an ellipse with axes ratio $e=\omega/f$, where the main axis points into the direction of the pressure gradient. Due to the lack of viscous damping in the nonturbulent layer above the BBL, velocities increase toward infinity if resonance is reached ($\omega=f$). The harmonic pressure term in (11) will be used below as a simple representation of tidal forcing in a rotating system

The situation becomes more complex inside the BBL due to the appearance of the internal pressure term $(b-b_\infty)\sin\alpha$ in (3), which represents the tendency of isopycnals to relax back to their equilibrium positions $(b=b_\infty)$. *Umlauf et al.* [2015] showed that the potential energy stored in the distorted near-bottom buoyancy field can be reversibly converted into kinetic energy of BBL motions, and vice versa, which implies the possibility of reversible BBL oscillations. The frequency of these oscillations is

$$\omega_c^2=f^2\cos^2\alpha+N_\infty^2\sin^2\alpha\,, \tag{14}$$

indicating that BBL resonance occurs for $\omega=\omega_c$ [*Umlauf and Burchard*, 2011]. Vice versa, if N_∞, f, and ω are considered to be given, BBL resonance will be observed if the slope α approaches the critical slope α_c found

Table 1. Standard Parameters Used for the Simulations in Sections 5 and 6

α	N^2_∞	f	z_0	τ_c	α_e
3×10^{-4}	6.5×10^{-4} s^{-2}	7.65×10^{-5} s^{-1}	10^{-3} m	10^{-4} m^2 s^{-2}	10^{-4} kg s^{-1} m^{-2}

from inverting (14). Model properties exhibit qualitative changes during the transition from subcritical to supercritical slopes, and some of the model assumptions break down near critical slopes [*Umlauf and Burchard*, 2011; *Schulz and Umlauf*, 2016].

For the location investigated in this study, the parameters N^2_∞, f, and α summarized in Table 1 (their derivation is discussed in more detail below). The frequency for critical boundary layer resonance derived from these parameters is $\omega_c=7.69\times10^{-5}$ s^{-1}, corresponding to a period of $T_c=22.7$ h. As discussed in more detail below, the proximity of T_c to the diurnal tidal period is one of the reasons why the diurnal tides are neglected in our model analysis.

Finally, for the following discussion of residual transports it is useful to note that *Umlauf and Burchard* [2011] showed that under the above conditions (harmonic forcing, zero mixing above the BBL), the residual upslope transport vanishes

$$\int_0^\infty \langle u \rangle dz = 0 , \tag{15}$$

where the angular brackets denote the average over one forcing period $T=2\pi/\omega$.

3. Study Site and Methods

3.1. Study Site

In July 2011, hydrographic and turbulence microstructure measurements were performed near position S in the East China Sea (Figure 3). The study site was located at 31°44.9′ N, 125°50.0′ E on a mildly sloping continental shelf at approximately 68 m water depth. The inertial period at this latitude is $T_f=23.3$ h, only slightly larger than the resonance period of the BBL derived above ($T_c=22.7$ h). Based on a finite-element global ocean tidal model with a regionally refined numerical grid, *Lefevre et al.* [2000] showed that the East China Sea is subject to strong tidal motions with the four major constituents being: the principal lunar and solar tides, M_2 and S_2, with semidiurnal periods, and the lunisolar and principal lunar diurnal tides, K_1 and O_1, respectively. The M_2 tide is dominant here, about 3 times stronger than the second largest tidal component, the S_2. The two diurnal tides are of similar magnitude and about 4 times weaker than the M_2 component. Similar results were derived from observations of current velocity data at 31°45′ N, 127°25′ E (east of position S) [*Yoshikawa et al.*, 2012]. It should be noted that the inertial period is close to the periods of the diurnal tides, precluding a straightforward spectral distinction between diurnal tidal and near-inertial signals in a short time series.

Figure 3 illustrates that position S is located approximately 400 km away from the Changjiang river mouth, which by far forms the largest freshwater source in this region. *Endoh et al.* [2016] pointed out that this large spatial separation, and the fact that the less dense river water will mainly affect the near-surface layer during the thermally stratified summer period, suggests that the BBL at position S is unlikely to be dynamically influenced by freshwater runoff.

In the area of interest, the main axis of the bottom slope, i.e., the direction of maximum inclination, is orientated approximately 20° relative to the zonal direction (Figure 3b). To be consistent with the model geometry shown in Figure 2, we introduce a local coordinate system with the x and y axes pointing in the upslope and along-slope directions, respectively, as indicated in Figure 3b. Using an identical coordinate system, *Endoh et al.* [2016] showed that the along-slope density gradient is nearly negligible compared to the cross-slope gradient. They also found that the observed periodic density variations in the BBL were largely caused by the up and downslope advection of isopycnals due to the tides, which forms the most important prerequisite for the occurrence of slope-induced tidal straining (see Figure 1).

Echosounding data from the cruise (not shown) showed that the bathymetry exhibits a nearly perfectly linear slope in the x direction on horizontal scales of the order of a few tens of kilometers. According to these
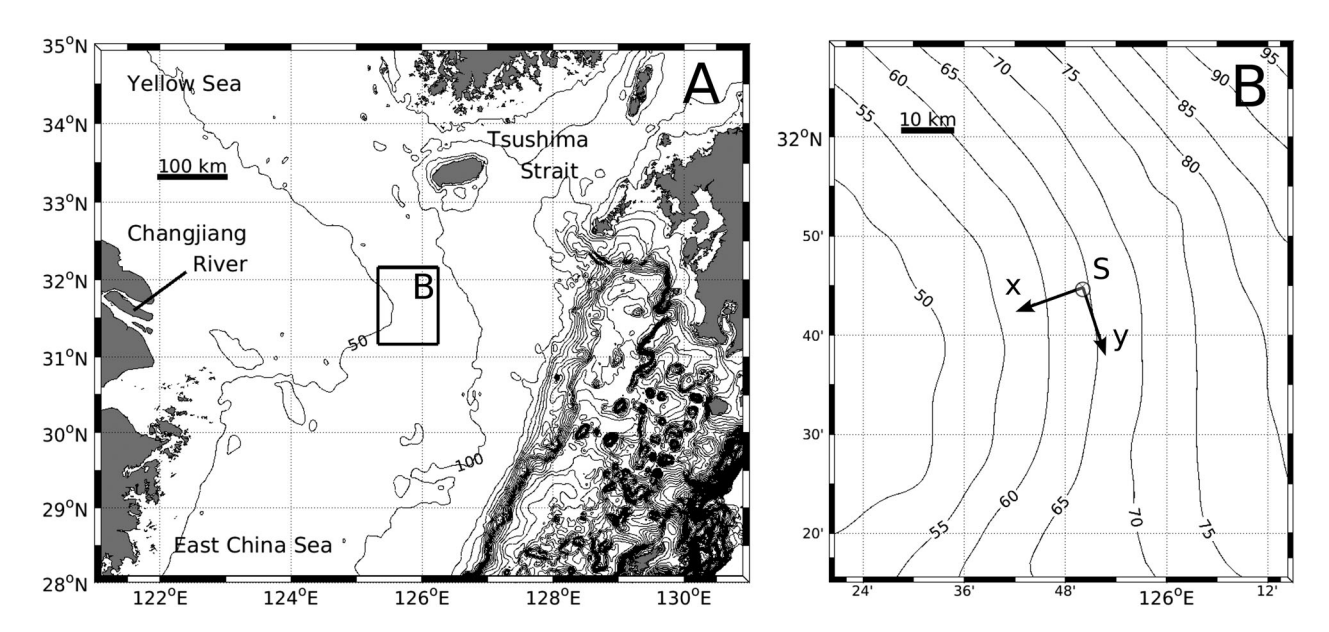
Figure 3. Maps of (a) East China Sea and (b) study area with deployment location "S." Local cross-slope and along-slope directions are denoted by *x* and *y* (rotated by 20° with respect to the zonal and meridional directions, respectively). Bathymetry is in meters, based on bathymetric data described in *Choi et al.* [2002].

data, the topographic slope is approximately 3×10^{-4}, which is also taken as the default value for the numerical simulations described below. Several bathymetric data sets for the East China Sea are available, but due to their coarse resolution the slope angle near position S tends to be somewhat overestimated. Recent topographic data discussed in *Choi et al.* [2002] suggests, e.g., a slope of nearly 6×10^{-4} near the study site. The sensitivity of our results with respect to these uncertainties in the slope angle will be discussed in Appendix A.

3.2. Methods

The data set we discuss here was collected with a 600 kHz ADCP (Workhorse from Teledyne RD Instruments) and a tethered turbulence microstructure profiler (TurboMAP-5 from JFE Advantech, Japan) during a cruise of the training ship Nagasaki-Maru in July 2011. Echo sounding data were obtained with a KFC-300 quantitative echo sounder from Sonic, Japan.

The ADCP was mounted on a trawl-resistant bottom frame and deployed on the seabed from 16:40 JST (Japan Standard Time) on 16 July 2011 to 15:40 JST on 21 July 2011. The vertical bin size was set to 1 m, and the depth of the first bin was located 3 m above the seabed, i.e., at approximately 65 m depth. The ADCP was operated in standard RDI "mode 1," sampling the along-beam velocities at a rate of 1.3 Hz during 20 min bursts starting every half hour. From the along-beam velocities averaged over 20 min (1600 pings), the horizontal components of the velocity were calculated at half-hour intervals.

The microstructure profiler was deployed from the ship within about 500 m distance from the ADCP between 17:00 JST on 17 July and 06:00 JST on 19 July. While the profiler was freely descending at a speed of 0.5–0.6 m s^{-1}, vertical shear and temperature microstructure was sampled at a rate of 512 Hz, whereas temperature, conductivity, pressure, turbidity, fluorescence, and the acceleration of the instrument were sampled at a rate of 64 Hz. A total of 101 profiles between a depth of 10 m and the bottom were obtained. From the microscale vertical shear, the dissipation rate of turbulent kinetic energy, ε, was estimated, assuming locally isotropic turbulence [*Hinze*, 1987] across 1 m windows as described in more detail in *Endoh et al.* [2016]. Series of one to three profiles taken approximately every hour were averaged to provide hourly means.

3.3. Analysis of Tidal Motions

Tidal forcing parameters for the idealized simulations described below were found by extracting the major tidal constituents from the velocities observed at position S. We performed this tidal analysis based on the velocity records at 30 m depth (38 m above the bottom), noting that results were not particularly sensitive
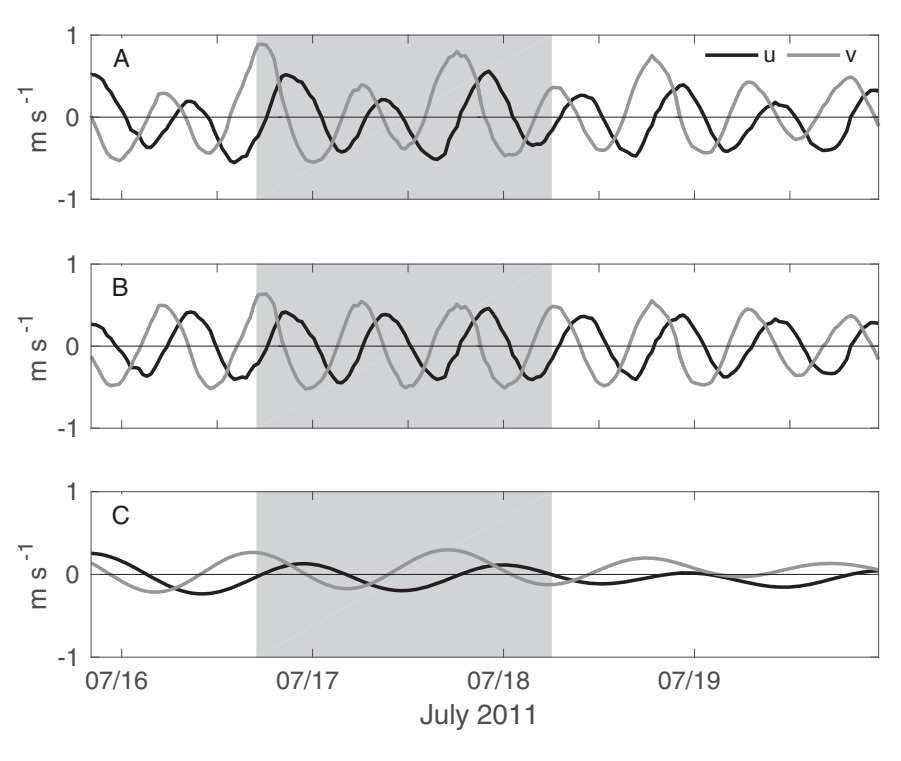
Figure 4. Time series of cross-slope (u) and along-slope (v) velocity components based on ADCP measurements in 30 m depth at position S: (a) unfiltered data, (b) highpass-filtered M_2 tidal currents, and (c) lowpass-filtered diurnal and subtidal currents. Period with microstructure measurements at position S is indicated in gray.

with respect to small variations of this parameter. This choice for the ADCP reference level was found to be a reasonable compromise between data quality (deteriorating with increasing distance from the ADCP) and our attempt to reduce the impact of bottom friction (increasing toward the bottom). Prior to the following analysis, the velocities were projected onto the topography-following x and y directions shown in Figure 3b.

To decompose the observed signals into semidiurnal and diurnal components, we used a phase-preserving high-order filter (equiripple FIR, 30 db stopband attenuation) with a cutoff frequency of 15 h. Comparison of the unfiltered (Figure 4a) and highpass-filtered semidiurnal velocities (Figure 4b) clearly shows that the currents at our study site were dominated by a regular M_2 tide with an amplitude of approximately 0.5 m s^{-1}, with slightly more energy in the along-slope direction. This tidal constituent explains approximately 83% of the total variance of the signal. The diurnal signal (Figure 4c) is substantially weaker and shows a decreasing magnitude during the observational period. A closer examination also reveals a frequency shift that is, however, not easily identified from the figure. Pure tidal motions are unlikely to exhibit such variability on a timescale of only a few days, suggesting that the observed signal is a mixture of near-inertial motions, which may quickly vary in time due to their direct dependence on the wind forcing, and different diurnal tidal constituents.
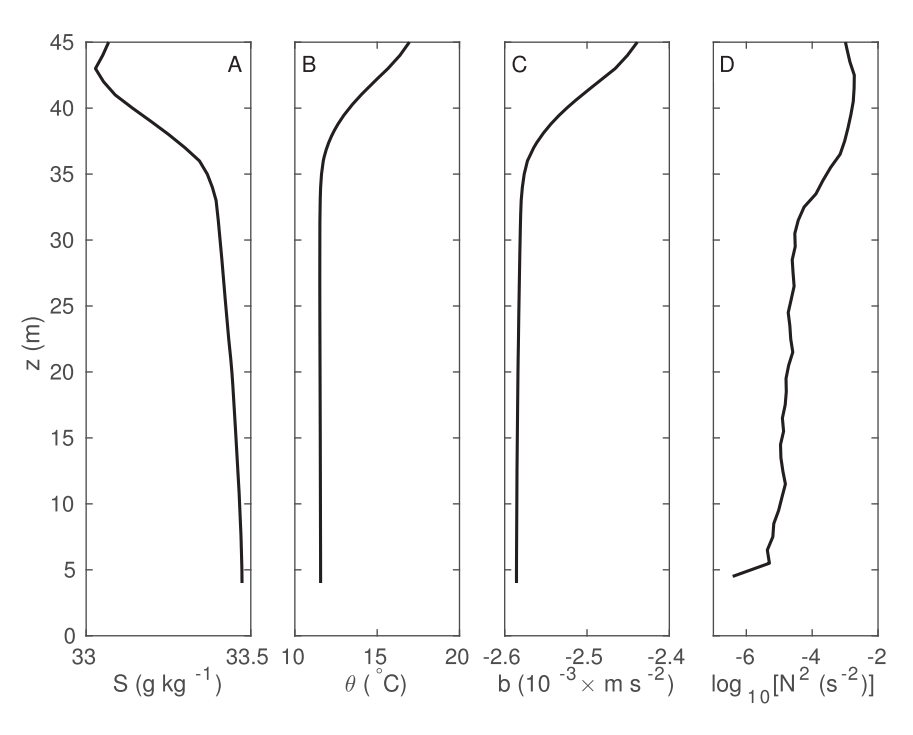
It is worth noting that a detailed tidal model of the East China Sea by *Xianwen et al.* [2001] yields a velocity amplitude of approximately 0.5 m s^{-1} for the M_2 component at position S, in good agreement with our data. For the diurnal K_1 tide, modeled velocity amplitudes were found to be around 0.1 m s^{-1}, approximately twice as large as those calculated for the O_1 constituent. Our observations (see Figure 4c) suggest that the model of *Xianwen et al.* [2001] slightly overestimates tidal motions in the diurnal frequency band.

4. Observations and Model Parameters

4.1. Observations

The observations at position S have been described in detail by *Endoh et al.* [2016]. Here we only summarize their main findings to provide the context for the discussion of the models results below.

Figure 5. Mean profiles of (a) salinity, (b) potential temperature, (c) buoyancy, and (d) buoyancy frequency squared. Profiles are based on the average of all available microstructure profiles at station S (gray-shaded period in Figure 4). The vertical axis, z, denotes the distance from the bottom (see Figure 2).
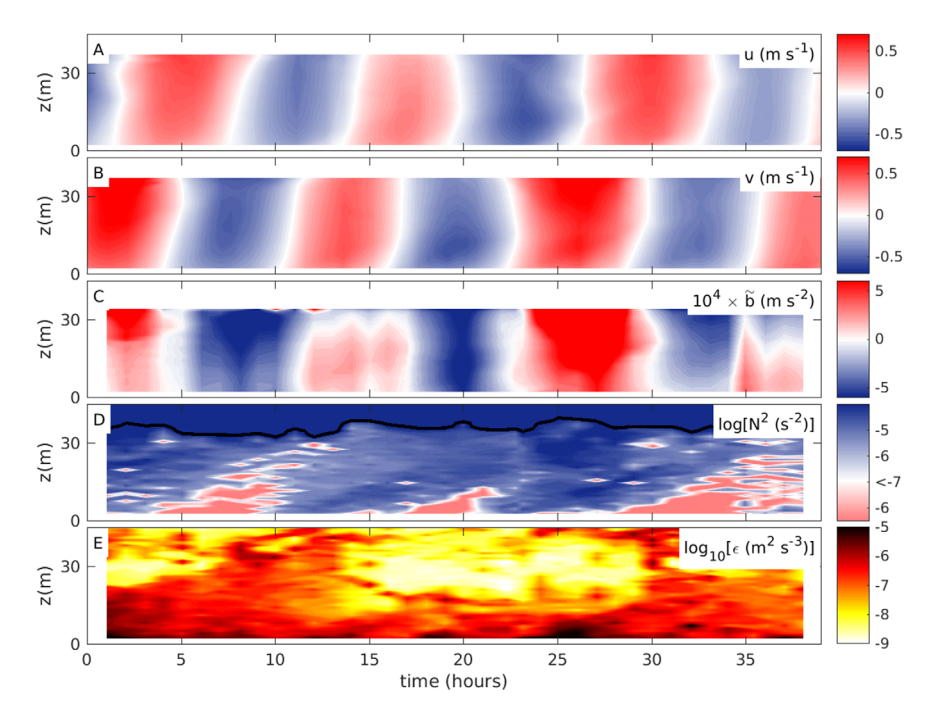
Figure 5 shows the averaged vertical structure of salinity S, potential temperature θ, potential buoyancy b, and the (square of the) buoyancy frequency N^2, based on the average of all profiles obtained at position S. Here we define the buoyancy as $b = -g(\rho_\theta - \rho_0)/\rho_0$, where ρ_θ is potential density and $\rho_0 = 1000$ kg m^{-3} a constant reference density. The figure shows that the lower part of the water column is characterized by a nearly well-mixed BBL of more than 35 m thickness, capped by a strongly stratified "interior" region with approximately linear stratification, slightly larger than $N^2 = 10^{-3}$ s^{-2}. Inside the BBL, the average stratification is 1–2 orders of magnitude smaller compared to this interior region (Figure 5d).

As already discussed in the context of Figure 4, BBL velocities are dominated by regular M_2 tidal motions, however, with a significant diurnal modulation and indications for a frictional reduction of the tidal velocities toward the bottom (Figures 6a and 6b). Also, the buoyancy anomaly $\tilde{b} = b - \langle b \rangle$, where $\langle b \rangle$ denotes the tidally averaged buoyancy shown in Figure 5c, is characterized by a clear M_2 tidal variability with a $\pi/2$ phase lag with respect to the u-component (Figure 6c). This phase shift is expected if buoyancy variations are due to advection of a constant cross-slope buoyancy gradient as mathematically described by (5).

In the context of the present study, the most interesting feature in these observations is the periodic destabilization of the lower part of the BBL (Figure 6d) that *Endoh et al.* [2016] showed to be consistent with slope-induced tidal straining as delineated in Figure 1. These unstable regions appear at the M_2 tidal frequency, exhibit a significant vertical phase shift, and affect a large fraction of the BBL. Beyond the key role played by the M_2 tidal currents in this processes, a diurnal suppression of the vertical extent of the unstable regions is also visible in Figure 6d, which should be kept in mind when interpreting the model results below (the diurnal signal is neglected in our model forcing).

Despite the dominant M_2 tidal forcing, the turbulence dissipation rates shown in Figure 6e do not exhibit a clear tidal signal. This is easily understood from the fact that the near-bottom velocity vector at position S essentially rotates at the M_2 tidal frequency without large modulations in magnitude (Figure 4c), different from previous field studies in regions with more rectilinear tides [e.g., *Simpson et al.*, 2002; *Burchard et al.*, 2002]. Noticeable is therefore in particular a diurnal modulation of the dissipation rate. Y. Wakata et al. (Transformation and disintegration of strongly nonlinear internal waves by topography in stratified lakes,

Figure 6. Evolution of observed (a) cross-slope velocity, (b) along-slope velocity, (c) buoyancy fluctuations, (d) buoyancy frequency, and (e) turbulence dissipation rate. Note the special logarithmic color scale in Figure 6d: for $N^2 < 0$ (unstable stratification), the value of $|N^2|$ is plotted in red shading, whereas regions with positive N^2 are plotted in blue shading. The black line indicates values of $N^2 = 10^{-3.7}$ s^{-2} and marks the vertical extent of the BBL. The time axis starts on 17 July 16:00 JST.

submitted to *Continental Shelf Research*, 2016) argue that this modulation is related to the vertical shear caused by the interference between diurnal and semidiurnal tidal currents rather than to the lateral advection of stratification in the upper part of the BBL, as originally proposed by *Endoh et al.* [2016].
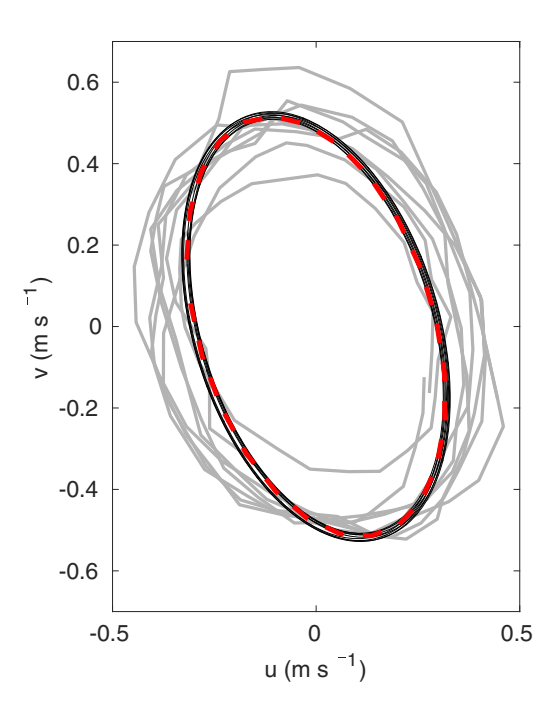
4.2. Model Parameters

The solution of the system of equations in (3)–(7) depends on a number of model parameters that determine: the properties of the rotating fluid (f, N_∞), the slope angle and the bottom roughness (α, z_0), and the tidal forcing (P_x, P_y). In addition, if the transport of suspended material is considered, the erosion parameter α_e, the critical shear-stress τ_c, and the sinking speed w_s appearing (8) and (9) have to be specified.

Most obvious is the choice of the Coriolis parameter ($f = 7.65 \times 10^{-5}$ s^{-1}) and the bottom slope ($\alpha = 3 \times 10^{-4}$), which can be determined without further assumptions from the local latitude and the echo sounding data obtained during the cruise, respectively (see above). As the bottom roughness is not well constrained, we chose a standard value here ($z_0 = 0.001$ m) and discuss the sensitivity of our results with respect to this parameter in Appendix A.

The determination of the time-dependent forcing functions $P_x(t)$ and $P_y(t)$ is based on the following considerations. First, we require a purely monochromatic forcing as in (11) in order to allow the model to reach periodic conditions after an appropriate spin-up period to be able to compute well-defined tidal averages. Second, in view of the idealized nature of our model, we will focus on forcing functions that are as simple as possible but still sufficient to mirror all key features of the observed BBL dynamics. Also, as discussed above in the context of (14), the diurnal tidal components are close to the critical period, $T_c = 22.7$ h, which is likely to induce unphysical resonance effects in the modeled BBL.

With this rationale in mind, and recalling that the M_2 tide largely determines the observed velocity variance at our study site, we computed the forcing functions based on the amplitude and phase of a pure M_2 tide with period $T_{M_2} = 12.42$ h. We thus fitted a sinusoidal M_2 signal to the highpass-filtered velocity data shown in Figure 4b, using the standard least squares fitting procedure described in *Emery and Thomson* [2001], however, with the following difference: the axes ratio of the tidal ellipse was kept fixed at the value ω/f for consistency with the model solution in (12). This modified fitting procedure yields a tidal ellipse with a velocity

Figure 7. Highpass-filtered M_2 tidal currents at 30 m depth (light gray) and modeled velocities in the region above the BBL (black lines). The dashed red line indicates a fit to the data based on a tidal ellipse with prescribed axes ratio ω/f.

amplitude of 0.53 m s^{-1} along the major axis, which is rotated at an angle of 107° counter-clockwise with respect to the along slope direction (see Figure 7). The analytical solution is seen to slightly overestimate the observed ellipticity but provides otherwise a good representation of the data. It is worth noting that orientation and tidal amplitude are also consistent with the M_2 tidal ellipse found by *Xianwen et al.* [2001] near this position.

In the next step, we computed amplitude and phase of the pressure function P_n defined in (11) by inverting (12), using the observed velocity amplitude. Projecting the result onto the x and y directions finally yields the required pressure functions $P_x(t)$ and $P_y(t)$. As shown above, fully periodic model solutions for this type of pressure forcing correspond to the tidal ellipse described by (12) in the nonturbulent model region above the BBL. However, numerical tests have shown that transients (mainly inertial oscillations) generated during the abrupt start of the simulations do not decay in this region due to the lack of any physical damping mechanism. The problem can be strongly reduced (but not fully eliminated) by linearly increasing the periodic pressure forcing from zero to full amplitude over a period of 10 days. After a spin-up period of additional 40 days, the solutions become fully periodic inside the BBL (where transients quickly decay as a result of viscous damping) and nearly periodic in the undamped region above the BBL (see Figure 7). As we are only interested in the processes inside the BBL, small deviations from perfect periodicity above the BBL are of no consequence for the following analyses.

Finally, the relevant background stratification N_∞ can be conveniently computed from the cross-slope buoyancy gradient $\partial b/\partial x$, using the projection relation in (2). Here we estimate $\partial b/\partial x$ following *Endoh et al.* [2016], who noted that buoyancy fluctuations inside the nearly well-mixed BBL are largely determined by up and downslope advection. Thus, for this purpose, the buoyancy equation in (5) can be approximated as
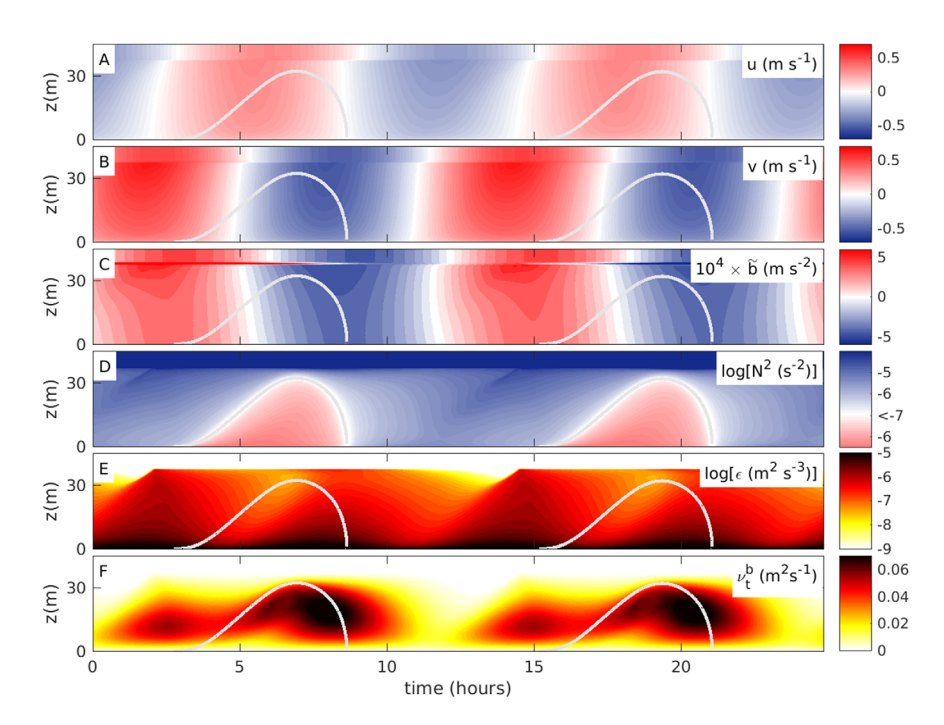
$$\frac{\partial b}{\partial t} = -u\frac{\partial b}{\partial x} \ , \qquad (16)$$

assuming that $\partial b/\partial x$ is constant.

Similar to *Endoh et al.* [2016], we find that $\partial b/\partial x = 2\times10^{-7}$ s^{-2} estimated from CTD measurements largely explains the observed buoyancy fluctuations due to cross-slope tidal motions (see below). According to (2), for the observed bottom slope, this value yields $N_\infty^2 \approx 7\times10^{-4}$ s^{-2}, slightly smaller than the measured vertical stratification above the BBL (Figure 5d) but of the correct order of magnitude. As pointed out by *Endoh et al.* [2016], the relevant interior stratification for slope-induced tidal straining is that *adjacent* to the BBL (i.e., in the interior region located at the same depth level as the BBL at position S) rather than *above* the BBL. It is likely that the real interior stratification adjacent to the BBL, rather than being vertically homogeneous as assumed in our model, slightly decays with depth away from the thermocline region.

5. Modeling Slope-Induced Tidal Straining

Using the periodic tidal forcing described in section 2.3, and the model parameters in Table 1, we investigate in the following to which extent our idealized model is able to reproduce the features of the observed BBLs. For easier comparison between field data (Figure 6) and model results (Figure 8), time axes have been aligned to reproduce the correct phase relationships in the M_2 tidal currents after the model has become

Figure 8. Evolution of modeled (a) cross-slope velocity, (b) along-slope velocity, (c) buoyancy fluctuations, (d) buoyancy frequency, (e) turbulence dissipation rate, and (f) turbulent diffusivity. Gravitationally unstable regions are indicated by gray lines in all panels. Axes ranges, color scales, and time axis are identical to those used in Figure 6.

periodically stationary. Due to their periodic nature, model results are only shown for two tidal periods for clarity.

The modeled velocities (Figures 8a and 8b) mirror the observed M_2 tidal variability with good accuracy but do not exhibit the observed diurnal modulation, which is obviously a consequence of neglecting the diurnal tidal constituents in our simulations. As explained above, the diurnal signal is significant but not essential for the process studied here. Similar to the observations, also the model results show clear indications for a frictional reduction of the velocities toward the bottom, which is an essential requirement for the development of SIPS.

Also, the magnitude and phase of the tidal buoyancy fluctuations shown in Figure 8c are in good agreement with the data, supporting the idea that the variability in buoyancy is largely a result of cross-slope advection as discussed above. The strong diurnal modulation of the buoyancy fluctuations in the upper part of the BBL found in the observations is, however, not represented by the model, as diurnal tides are ignored in our simulations.

While the good agreement between model and data regarding the tidal velocity and buoyancy fluctuations is largely a result of the selected forcing variables and model parameters, the correct prediction of BBL stratification provides a much more stringent test of the model performance. Figure 8d shows that the model provides an excellent representation of the evolution of BBL stratification in at least two important aspects. First, the predicted BBL thickness is approximately 37 m, and therefore well inside the observational range (see Figure 6d). In view of the complex interplay between slope-induced restratification and mixing that determines the BBL thickness, this is a remarkable result. Second, the model is also able to reproduce the periodic generation and destruction of stratification (SIPS) inside the BBL, in particular regarding the occurrence of gravitationally unstable layers during periods of upslope flow. The observed and modeled unstable layers have a similar vertical extent and timing but, different from the model, the observations also exhibit a strong diurnal modulation of stratification that leads to a suppression of the convective layer thickness during every second instance of their occurrence (e.g., at $t \approx 20$ h in Figure 6d), which cannot be reproduced in the model, of course, again because diurnal tides are ignored.

As pointed out above, the imprint of this diurnal modulation in stratification is also clearly visible in the observed dissipation rates (Figure 6e) but, for the reasons described above, cannot be reproduced by the

model. The model does, however, correctly predict the strong increase of the dissipation rates toward the bottom, and the correct order of magnitude of dissipation at the beginning and end of the observation period (Figure 8e). Modeled dissipation rates show a M_4 periodicity with a M_2 modulation that reflects the ellipticity of the tidal currents: largest dissipation rates are found at peaks of the v component, which dominates the M_2 tidal motions (see above).

While the variability in the modeled dissipation rates is therefore mainly driven by variations in tidal forcing, the eddy diffusivities shown in Figure 8f are also strong affected by variations in stratification associated with SIPS. Although peaks in dissipation rate and eddy diffusivity approximately coincide, the latter shows a much stronger tidal asymmetry: largest diffusivities are found during periods of upslope flow, when slope-induced tidal straining reduces vertical stratification, or even causes regions with negative N^2. We will see in the following that this modulation of the eddy diffusivity is essential for the generation of residual transports.

6. Dynamics of Suspended Material

One of the most important implications of tidal straining is the generation of residual currents and residual transports of dissolved substances and suspended material. *Endoh et al.* [2016] speculated that this process may also play an essential role for the transport of suspended material at their study site in the East China Sea. Although their turbidity measurements (see their Figure 2i) clearly show strongly enhanced concentrations of suspended material inside the BBL, their data were too limited to draw any definite conclusions about residual SPM transports. In the following, we therefore discuss a number of idealized simulations to clarify the mechanisms and potential implications of slope-induced tidal straining for the residual transport of suspended material.
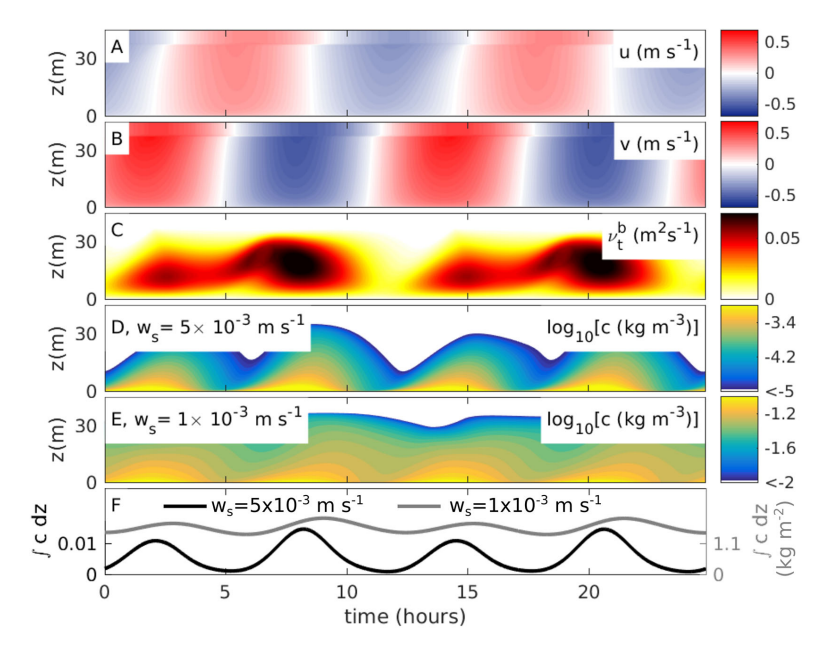
6.1. Temporal Variability

Our simulations are based on the SPM transport equation in (8) and the simple erosion model in (9). Lacking information about sediment properties at the study site, we vary the sinking speed, identified by *Schulz and Umlauf* [2016] as the key parameter determining the transport of suspended material, over a broad range of values. For the critical shear stress, τ_c, and the erosion parameter, α_e, shown to be of only secondary importance by *Schulz and Umlauf* [2016], we adopt the standard values suggested by these authors (see Table 1).

Figures 9d and 9e reveal for two different sinking speeds that maxima in the SPM concentrations follow maxima in the turbulence diffusivities with a small phase shift, which mirrors the time required to mix eroded material up into the BBL. Concentration maxima are found when the cross-slope velocity u is close to zero (Figure 9a), or, likewise, when the magnitude of the more energetic along-slope flow component v attains maximum values (Figure 9b). Tidal asymmetries resulting from the modulation of the turbulent diffusivity due to SIPS are clearly evident in both local and vertically integrated SPM concentrations (Figures 9d–9f). For large sinking speeds (Figure 9d), highest concentrations are found at the end of the period with upslope flow, when turbulent diffusivities are maximum, along-slope velocities close to their maximum negative values ($v < 0$), and cross-slope velocities close to zero. Similar SPM maxima are also found at the end of downslope flow period, however, with significantly smaller concentrations due to the comparably smaller turbulent diffusivities.

The strong correlation between high SPM concentrations and negative along-slope speeds constitutes a tidal pumping mechanism that, as discussed in more detail below, leads to a vigorous residual transport of suspended material along the slope in the negative y direction. Tidal pumping is much less effective in the cross-slope x direction because SPM concentration maxima are associated with minima in the magnitude of the cross-slope velocity ($u \approx 0$). Although tidal asymmetries in SPM concentrations can also be discerned for the case with low sinking speeds (Figures 9e and 9f), they are less pronounced, and their potential to trigger tidal pumping is therefore expected to be weaker.

Finally, it is worth noting that the collapse of cross-slope tidal pumping mentioned above is qualitatively different from the nonrotating case investigated by *Schulz and Umlauf* [2016]. Although their simulations showed similar tidal asymmetries with highest turbulent diffusivities and SPM concentrations observed during periods of upslope flow, these maxima occurred earlier compared to the rotating case. This is easily

Figure 9. Evolution of (a) cross-slope velocity, (b) along-slope velocity, (c) turbulent diffusivity, and (d, e) SPM concentrations for two different settling velocities: $w_s = 5 \times 10^{-3}$ m s^{-1} and $w_s = 1 \times 10^{-3}$ m s^{-1}. Figure 9f shows the corresponding integrated SPM concentrations. Figures 9a–9c are redrawn from Figures 8a, 8b, and 8f for better orientation.

understood from the fact that in the nonrotating case the v component, dominating BBL turbulence in our case, is lacking, and highest diffusivities are thus observed significantly before the upslope flow reversal. In the nonrotating case, high SPM concentrations are therefore correlated with significant upslope velocities ($u > 0$), resulting in an effective upslope pumping of suspended material.

6.2. Residual Transports

The residual transports of suspended material in the cross-slope and along-slope directions are defined as

$$F_x = \langle uc \rangle - \langle c \rangle w_s \sin \alpha , \quad F_y = \langle vc \rangle , \tag{17}$$

where the angular brackets denote the tidal average. The second term in the cross-slope flux F_x represents the small downslope motion of vertically sinking material near a sloping bottom. *Schulz and Umlauf* [2016] showed that this term is generally negligible for small slopes ($\alpha \ll 1$), and therefore will be ignored in the following.
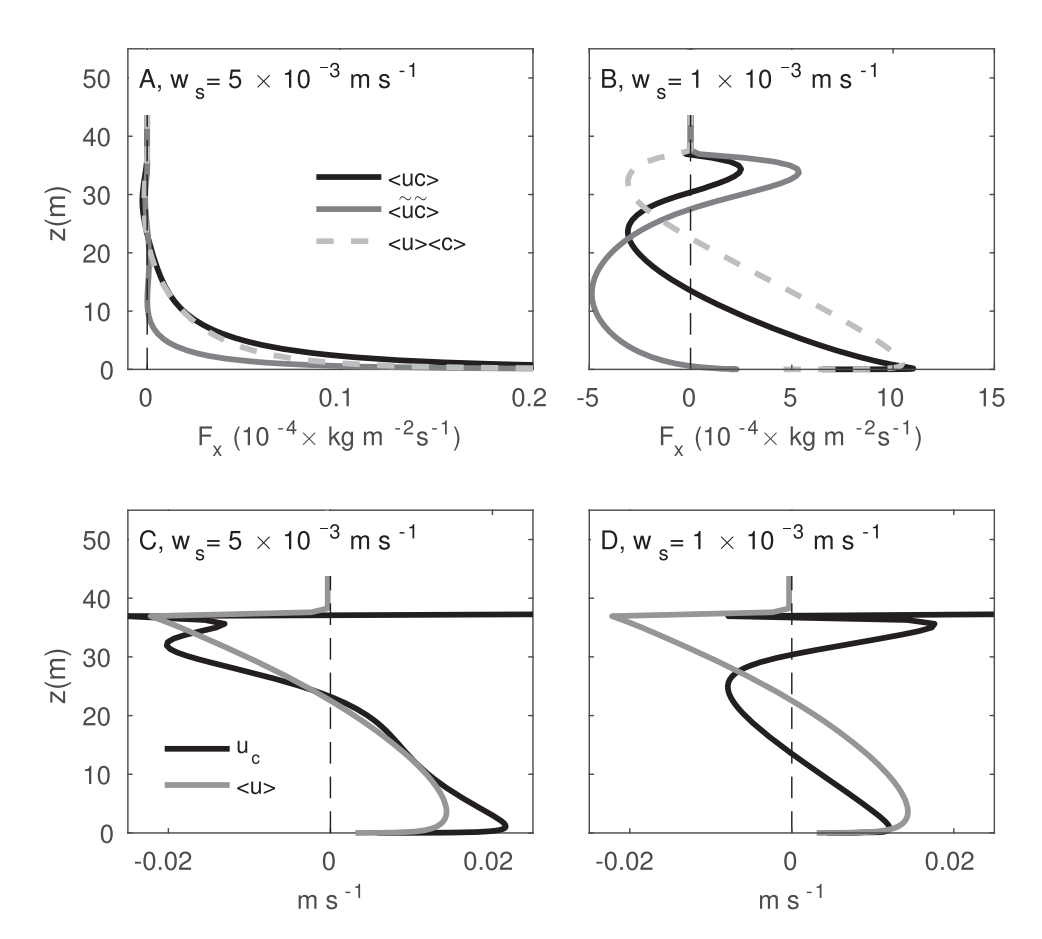
Schulz and Umlauf [2016] also pointed out that the fluxes defined in (17) are of limited use for the analysis of the tidal transport mechanisms due to their direct dependency on the SPM concentrations. Instead, they suggested to normalize the SPM fluxes with the concentrations, which removes this dependency

$$
\begin{aligned}
u_c &= \frac{\langle uc \rangle}{\langle c \rangle} = \langle u \rangle + \frac{\langle \tilde{u}\tilde{c} \rangle}{\langle c \rangle} , \\
v_c &= \frac{\langle vc \rangle}{\langle c \rangle} = \langle v \rangle + \frac{\langle \tilde{v}\tilde{c} \rangle}{\langle c \rangle} .
\end{aligned}
\tag{18}
$$

The normalized velocities u_c and v_c are recognized as the effective velocities at which SPM is transported across and along the slope during a tidal cycle. In the second step in (18), we have further decomposed all quantities into tidal averages and fluctuations (denoted by the tilde), revealing that the transport velocities are the sum of the residual velocities and correlation terms representing the effect of tidal pumping.

Figures 10 and 11 compare cross-slope and along-slope SPM fluxes for the two sinking speeds shown in Figures 9d and 9e. As already speculated in section 6.1, for the larger sinking speed the contribution of tidal pumping to the total cross-slope flux is small due to the fact that high SPM concentrations generally co-occur with negligible cross-slope speeds (Figure 10a). This is confirmed by Figure 10c, showing that the transport velocity u_c is of the same order of magnitude as the residual current $\langle u \rangle$. Different from the
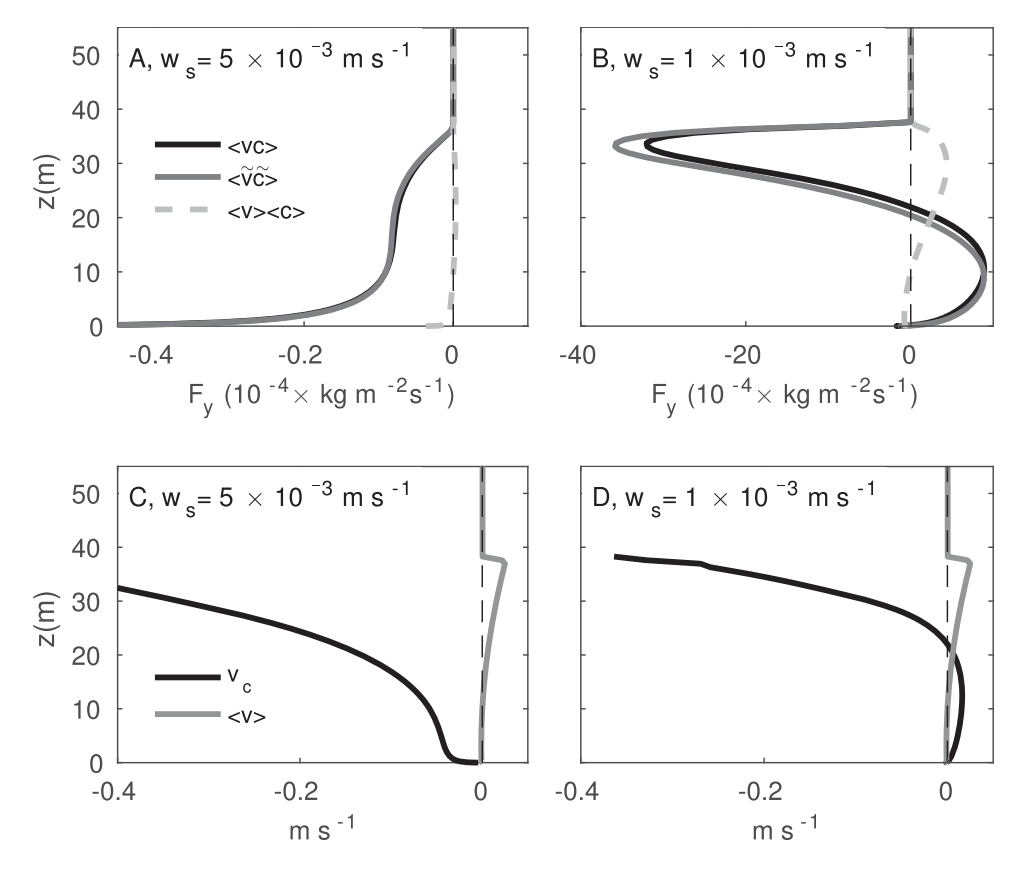
Figure 10. Residual cross-slope fluxes of suspended material for settling velocities (a) $w_s = 5 \times 10^{-3}$ m s^{-1} and (b) $w_s = 1 \times 10^{-3}$ m s^{-1} with contributions from the residual currents and tidal pumping as indicated. Figures 10c and 10d show the corresponding effective transport velocities defined in (18). Note the different axes ranges.

nonrotating case investigated by *Schulz and Umlauf* [2016], tidal pumping is therefore not the dominating process in this example. This is also true for the case with a small sinking speed (Figures 10b and 10d), which is, however, further complicated by the fact that the contributions of the residual current and tidal pumping may point into different directions.

The situation changes completely if the along-slope fluxes are considered. Figures 11a and 11b show that for both sinking speeds tidal pumping provides the overwhelming contribution to the net SPM fluxes. The strong correlation between large SPM concentrations and negative along-slope velocities for the case with a large sinking speed (see section 6.1) induces a residual flux of suspended material in the negative y direction that is almost 1 order of magnitude larger than the corresponding cross-slope flux (Figure 10a). The effectiveness of tidal pumping in this case is corroborated by Figure 11c, showing that the contribution of the residual current to the effective transport velocity v_c is generally negligible. Typical transport velocities in the lower part of the BBL, where SPM concentrations are high, are of the order of 0.1 m s^{-1}, suggesting that suspended material is transported approximately 5 km along the slope during one tidal cycle.

Particularly notable is the two-layer structure determining the along-slope SPM transport for the case with a low sinking speed (Figure 11b), which may be explained as follows. Comparing along-slope velocities and SPM concentrations in Figures 9b and 9e shows that during periods of positive along-slope flow, near-bottom SPM concentrations are highest because stable stratification prevents resuspended material to be diluted by mixing across a larger fraction of the BBL. The opposite is the case for periods with negative along-slope flow. Here SPM is mixed up high into the BBL, because mixing is not suppressed by stable stratification any more. The net effect of the resulting correlations is a positive along-slope transport near the bottom, and a negative transport in the upper part of the BBL.

Figure 11. As in Figure 10, but now for the along-slope SPM fluxes and transport velocities. Note that the axes ranges are different from Figure 10.
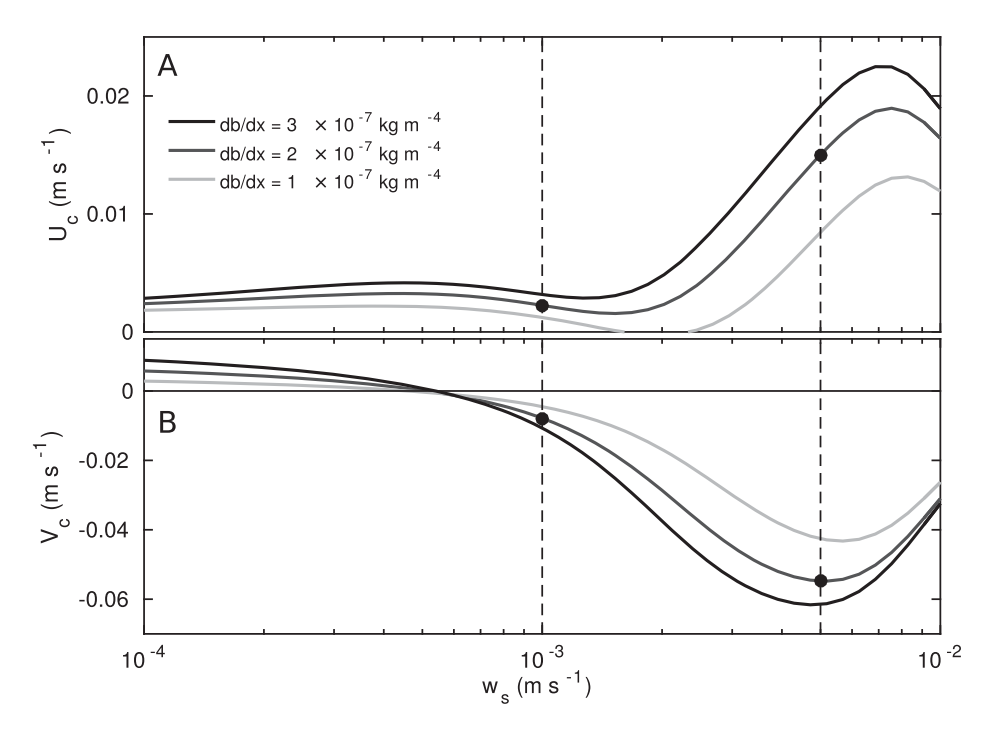
6.3. Variable Sinking Speed and Stratification

To quantify the variability of SPM transport across a larger parameter space, it is useful to introduce the normalized integrated fluxes,

$$U_c = \frac{\int \langle uc \rangle dz}{\int \langle c \rangle dz} \,, \qquad V_c = \frac{\int \langle vc \rangle dz}{\int \langle c \rangle dz} \,. \tag{19}$$

Analogous to the vertically variable transport velocities u_c and v_c, the vertically integrated expressions in (19) define bulk measures for the residual velocities at which SPM is transported across and along the slope, respectively [*Schulz and Umlauf*, 2016].

In Figure 12, the distribution of U_c and V_c for varying settling velocities is displayed. As already discussed in section 6.2, the cross-slope sediment flux is largely determined by the contribution of the residual current, $\langle u \rangle \langle c \rangle$, which is directed upslope near the bottom and downslope in the upper part of the BBL. The contribution of tidal pumping is either relatively small (for large sinking speeds, see Figures 10a and 10c), or even counteracts the contribution of the residual current (for small sinking speeds, see Figures 10b and 10d). The local maximum in U_c for $w_s \approx 7 \times 10^{-3}$ m s^{-1} (Figure 12a) can thus be explained as follows. For settling velocities higher than this optimal value, suspended matter remains inside a thin near-bottom layer, where flow velocities are strongly reduced due to frictional effects. SPM transport is not efficient in this case. Material that exhibits settling velocities smaller than the optimal value is more homogeneously distributed across the BBL, implying that the near-bottom upslope transport is partly compensated by a downslope transport in the upper part of the BBL. The local minimum, visible Figure 12a for sinking speeds slightly larger than $w_s = 10^{-3}$ m s^{-1}, originates from the effect of tidal pumping, opposing the contribution of the residual current for material with small settling velocities (see Figure 10b). It is remarkable that for virtually all settling velocities investigated here, the transport is directed upslope, similar to the nonrotating case studied by *Schulz and Umlauf* [2016].

Figure 12. Distribution of (a) cross-slope and (b) along-slope transport velocities, U_c and V_c, for variable settling velocities and cross-slope buoyancy gradients (all other parameters as in Table 1). Dashed vertical lines indicate the standard cases of small and large settling velocities discussed in the context of Figure 9.
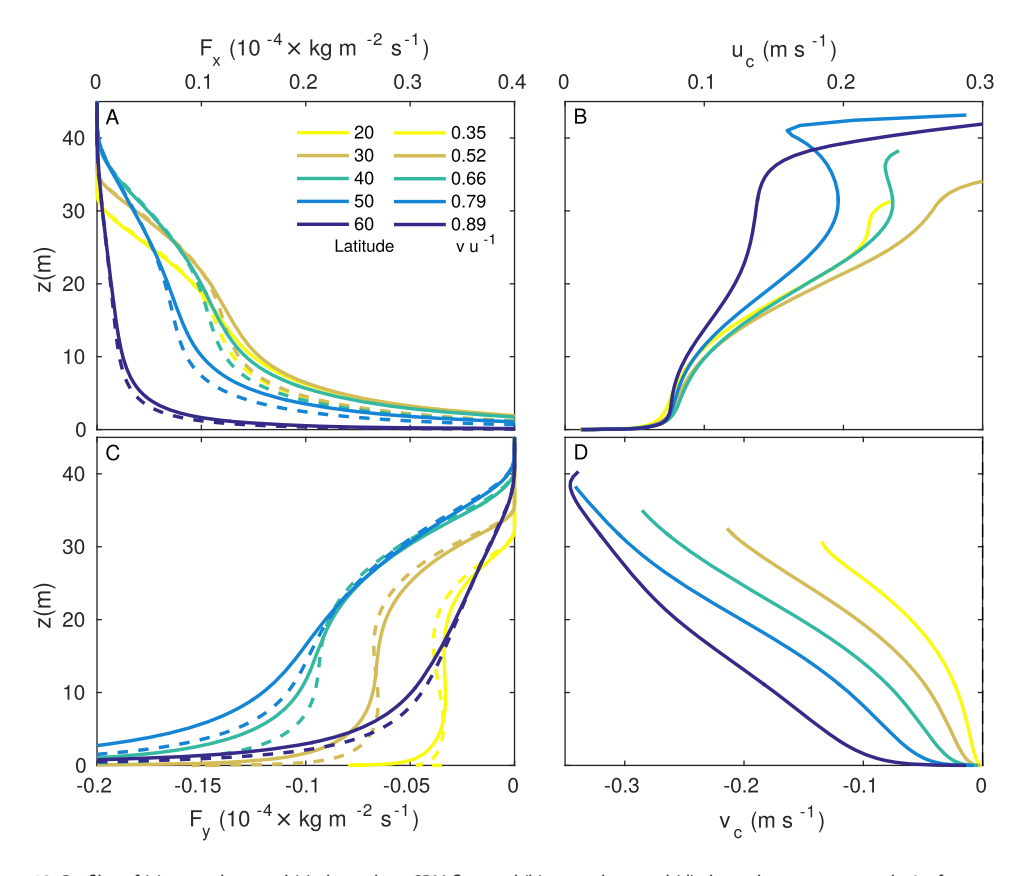
Different from the cross-slope transport of suspended material, the along-slope transport is mainly determined by tidal pumping (Figure 11). In this case, V_c reaches a local minimum (maximum negative transport rates) near $w_s \approx 5 \times 10^{-3}$ m s^{-1}. This optimum value is also marked in Figure 12 and corresponds to the case of large sinking speed discussed in the previous sections. The maximum in the transport rate for this value of the sinking speed is shaped by two competing effects. For settling velocities larger than the optimum value, suspended material is largely located inside the thin frictional near-bottom layer, where tidal pumping is not effective and V_c thus decreases. For material sinking slower than the optimal value, the negative near-bottom transport is partly compensated by an opposing transport in the upper part of the BBL (see, e.g., Figures 11a and 11b which are indicated in Figure 12b). If sinking speeds are small enough, this effect may even cause a reversal of the transport direction (Figure 12b). Comparing the magnitudes of U_c and V_c in Figure 12, it is evident that along-slope tidal pumping results in a factor of 2–3 larger transport velocities compared to the cross-slope direction.

Finally, it is worth noting that Figure 12 also reveals that stronger background stratification enhances the SPM transport mechanisms in both the cross-slope and along-slope directions. This is expected, however, as stratification is one of the prerequisites for slope-induced tidal straining and pumping. The existence of an optimal settling velocity for upslope transport, and the observed dependency on background stratification, are in agreement with the findings of *Schulz and Umlauf* [2016] for the nonrotating case.

6.4. Rotational Effects

According to (12) and (13), the shape of the tidal ellipse is determined by the Coriolis parameter, which is therefore likely to have an important impact on tidal straining and SPM transport. In the following, we investigate this effect in a series of simulations with varying latitude (varying Coriolis parameter), leaving all other parameters as in Table 1. For the sinking speed, we assume $w_s = 5 \times 10^{-4}$ m s^{-1}, corresponding to the optimal value for along-slope tidal pumping identified in the previous section.

We consider two special cases for the pressure forcing in (11). In the first case, we assume that the pressure force is directed exactly in the cross-slope direction ($P_x \neq 0$, $P_y = 0$), whereas in the second case the forcing is purely along-slope ($P_x = 0$, $P_y \neq 0$). Using the analytical solution in (12), we adjust the pressure force P for each case exactly such that the velocity amplitude in the direction of the forcing remains constant at a
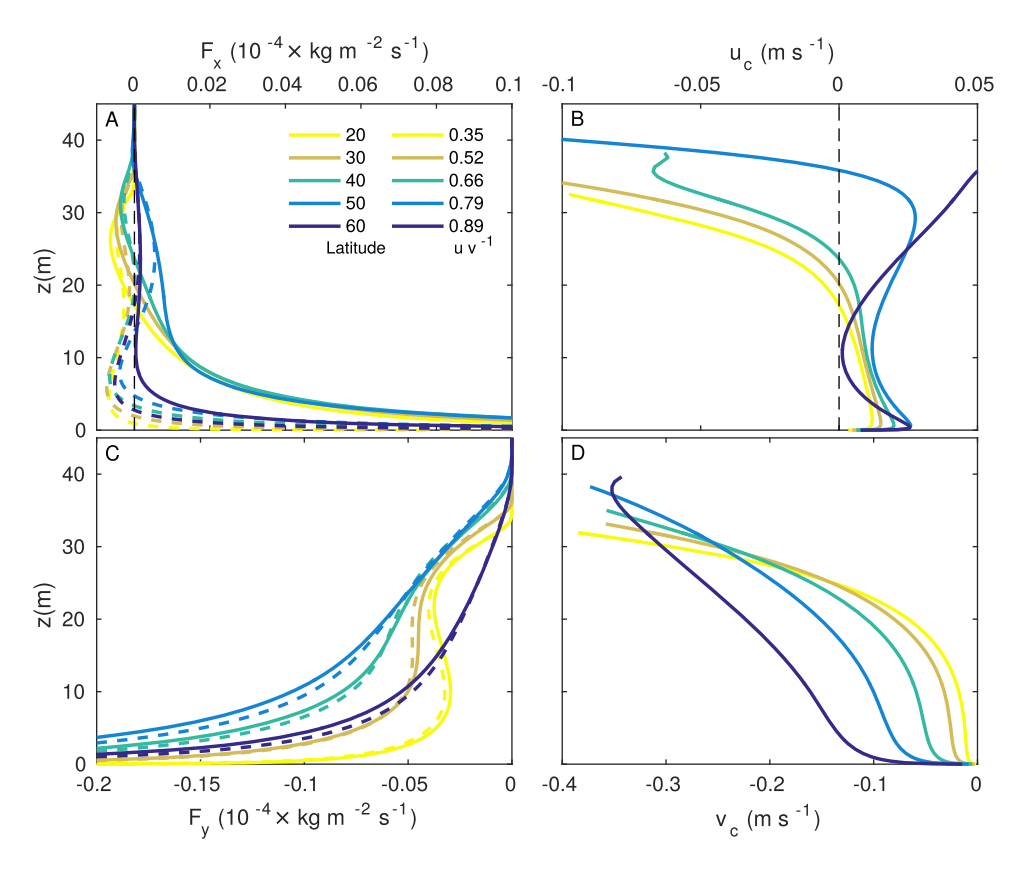
Figure 13. Profiles of (a) cross-slope and (c) along-slope SPM flux, and (b) cross-slope and (d) along-slope transport velocity for a range of latitudes between 20°N and 60°N (at 10° intervals). The pressure forcing is purely cross-slope ($P_y = 0$), and the amplitude of the cross-slope tidal velocity fluctuations in the region above the BBL is $u = 0.5$ m s^{-1} for all cases. The amplitude of the corresponding along-slope component v increases with latitude as indicated. Dashed lines in Figures 13a and 13c show the contribution of tidal pumping to the overall SPM flux.

value of 0.5 m s^{-1}. This results in a tidal ellipse with the (constant) major axes oriented parallel to the pressure force (i.e., either cross-slope or along-slope), and the minor axes increasing in magnitude with increasing Coriolis parameter. The latter is varied by changing the latitude from 20°N to 60°N at 10° intervals, corresponding to axes ratios between 0.35 and 0.89 for the tidal ellipses. Using (14), it is easy to show that for the parameters in Table 1, BBL resonance and the transition to supercritical slopes [see *Schulz and Umlauf*, 2016] occur at a latitude of approximately 75° N. The range of latitudes used here guarantees that BBL resonance does not affect the results.

The case with pure cross-slope forcing ($P_y = 0$) includes the nonrotational case ($f = 0$, $v = 0$) investigated in detail by *Schulz and Umlauf* [2016]. As pointed out by these authors, the turbulent diffusivities show in this case a clear M_4 signal that exhibits a M_2 modulation due to SIPS (higher diffusivities are observed during periods with upslope flow). These tidal asymmetries trigger an efficient tidal pumping mechanism that transports suspended material in the upslope direction. Figures 13a and 13b show that this mechanism remains essentially unchanged for latitudes up to approximately 40°N, corresponding to axes ratios of up to 0.66 for the tidal ellipse (note that the nonrotating case discussed by *Schulz and Umlauf* [2016] is not shown in the figure). While the BBL thickness significantly increases over this range of latitudes, SPM fluxes and transport velocities exhibit only small changes in the lowest 20 m of the BBL, where most of the suspended material is located and therefore most of the transport occurs. Quite differently, the along-slope SPM transport, vanishing for $f = 0$, quickly increases for $f > 0$ as a result of the same tidal pumping mechanisms described in detail in sections 6.1 and 6.2 (see Figures 13c and 13d).

For higher latitudes, the tidal ellipses gradually approach a circular shape, implying that the magnitude of the rotating velocity vector changes only slightly during a tidal cycle. As consequence, the turbulent diffusivity and the bottom stress (both important for SPM erosion) show a transition from a pronounced M_4

Figure 14. As in Figure 13, but now for along-slope pressure forcing ($P_x = 0$), and constant amplitude of the along-slope tidal velocity fluctuations ($v = 0.5$ m s^{-1}).

variability with two maxima during a tidal cycle toward a weak M_2 modulation with a single maximum during periods with upslope flow. This single maximum is also much less pronounced, and thus considerably less material is eroded compared to the cases with smaller rotation rates. Therefore, although tidal pumping is still active or even increasing in the along-slope direction (see Figure 13d), the total SPM fluxes collapse for high latitudes (Figures 13a and 13c).

In our second series of simulations (Figure 14), we assume that the tidal pressure force is directed exactly along the slope ($P_x = 0$). Different from the case with cross-slope forcing, both the cross-slope and the along-slope SPM fluxes vanish in the limit $f \rightarrow 0$ for symmetry reasons (this trivial case is not shown in the figure). For increasing latitudes, a weak upslope transport develops, which, similar to the example in section 6.2, is driven by the residual flow rather than by tidal pumping (Figures 14a and 14b). The weak transport rates in the cross-slope direction are strongly contrasted by the vigorous along-slope tidal pumping mechanism that quickly develops for increasing f (Figures 14c and 14d). The mechanisms are analogous to the example discussed in the previous sections (see Figures 11a and 11c), which was also characterized by a dominant along-slope flow component. For the highest latitudes, however, both the cross-slope and along-slope transports collapse again due to decreasing concentrations of suspended material. The reasons are identical to those discussed above.

7. Discussion and Conclusions

Two main conclusions can be drawn from the first part of our study, which showed that an idealized one-dimensional numerical model is able to reproduce the most important features in a data set describing tidal straining on a sloping shelf in the East China Sea. First, the good agreement between model and data indicates that the model correctly represents the key physical processes determining slope-induced tidal straining; and second, our results let it seems unlikely that processes other than those represented in the model (e.g., classical tidal straining due to river runoff) explain the observed BBL variability. The combination of

model results and experimental data therefore provides the first direct and conclusive evidence for the occurrence of slope-induced tidal straining at a real ocean site.

Our simulations also revealed a number of important processes related to the effect of rotation, which was ignored in previous studies of slope-induced tidal straining. For tidal ellipses oriented in the cross-isobath direction, the upslope transport of suspended material by tidal pumping, originally described by *Schulz and Umlauf* [2016] for the nonrotating case, was only slightly modified by rotational effects. However, the along-slope tidal velocity fluctuations induced by these rotational effects were shown to trigger a new type of tidal pumping mechanism that efficiently transports suspended material along the slope. In the case of tidal ellipses orientated in the along-isobath direction, along-slope tidal pumping was of magnitude comparable to the case with cross-slope forcing.

In both cases, tidal pumping was found to be most efficient for an optimal sinking speed that was of the order of 5×10^{-4} m s^{-1} in our example. For material sinking significantly slower or quicker than this value, the tidal pumping of suspended material was strongly reduced. Typical transport velocities deduced from our simulations suggest that suspended material may be transported over several kilometers along the slope during one tidal cycle. It should be noted that these large transport rates do not result from the combination of temporal settling lags and tidal asymmetries induced by overtides [e.g., *Groen*, 1967], which are ignored in our idealized study.

Our results exhibit a number of similarities with previous investigations of SPM transport due to classical tidal straining. For the cases with cross-slope tidal forcing, SPM is transported up the slope by the same tidal pumping mechanisms that also determine up-estuary transport in classical tidal straining [*Scully and Friedrichs*, 2007; *Burchard et al.*, 2013]. However, there is one important difference. While in classical tidal straining the maximum layer thickness across which suspended material can be vertically distributed is naturally given by the (to first order) constant water depth, in slope-induced tidal straining the thickness of the suspension layer is limited by the maximum BBL thickness during a tidal cycle. The latter, however, is part of the solution, and therefore unknown a priori. Beyond this, in contrast to the water depth, the BBL thickness may exhibit large variations during a tidal cycle, which complicates the pumping mechanism. As discussed in detail by *Schulz and Umlauf* [2016] in the context of their Figure 7, these variations in BBL thickness, combined with the settling lag, trigger a different type of tidal pumping that may result in an effective reversal of the transports for steep slopes (these cases are, however, not considered in the present manuscript).

For along-slope forcing, the along-slope component of the velocity modifies the timing of the turbulent diffusivity peaks (compared to pure upslope forcing), leading to a decorrelation of the cross-slope velocity and SPM fluctuations. In this case, cross-slope tidal pumping collapses, and the upslope SPM transport is determined almost exclusively by the residual current, similar to the analytical solution for gravitationally driven SPM transport in estuaries [*Hansen and Rattray*, 1965; *Burchard et al.*, 2002]. Similar to these studies, we also find that larger $\partial b / \partial x$ and larger sinking velocities (larger Rouse numbers) induce larger SPM transports (except for extreme cases with very quickly sinking material).

Additional parameter studies have shown that the processes identified in this study are robust, and therefore likely to occur across a wide range of naturally occurring conditions. It should, however, be kept in mind that only the basic mechanisms of slope-induced tidal straining and SPM transports are represented by our idealized model. The most important limitation is perhaps related to the assumption of homogeneity of the cross-slope buoyancy gradient $\partial b / \partial x$ and slope angle α. This implies that the horizontal divergence of the SPM fluxes, which determines the local accumulation rates, cannot be directly derived from model results. Nevertheless, as discussed by *Schulz and Umlauf* [2016] in the context of their Figure 12, limited information about flux divergences and accumulation areas, e.g., in the vicinity of a thermocline or near abrupt changes in topography, can be obtained from the modeled variability of the SPM fluxes for variable $\partial b / \partial x$ and α. Obviously, however, a detailed account of the role of horizontal inhomogeneities requires two or three-dimensional modeling studies.

In contrast to classical tidal straining that relies on the existence of a freshwater source or differential heating, slope-induced tidal straining only requires: a slope, an oscillating tidal current, and a stratified water column. These prerequisites are nearly ubiquitous in the ocean.
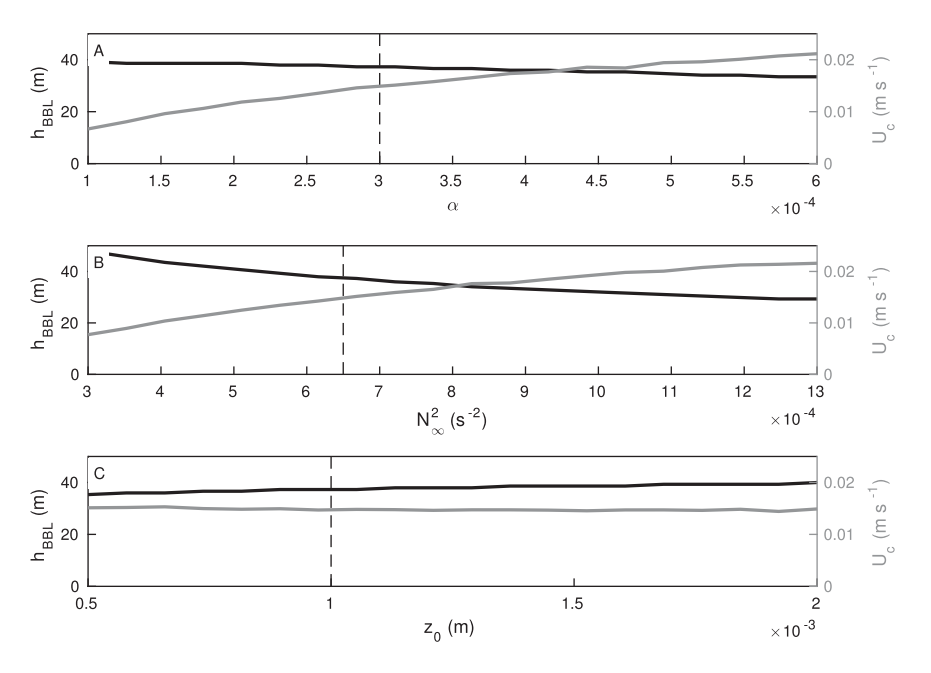
Figure A1. BBL thickness and bulk transport velocity as functions of (a) slope angle, (b) background stratification, and (c) bottom roughness. Standard parameters from Table 1 are indicated by vertical dashed lines.

Appendix A: Sensitivity With Respect to Other Model Parameters

Here we briefly discuss the sensitivity of our model results with respect to variations in model parameters that have not been investigated in detail above. To this end, we individually vary selected parameters, leaving all other parameters at their reference values compiled in Table 1. The target parameter for this sensitivity study will be the BBL thickness that is the product of the complex interplay between mixing and restratification processes, and therefore provides a simple but useful proxy for overall model performance.

Figure A1a shows that a factor-2 increase or decrease of the slope angle only results in a small (around 10%) change in the computed BBL thickness. Possible uncertainties in the slope angle are therefore of minor importance for the predicted BBL thickness. A factor-2 increase or decrease in background stratification (Figure A1b), however, induces significant changes in the BBL thickness, with deviations of up to 30% from the reference value. As our estimate of N_∞^2 is based on the cross-slope buoyancy gradient $\partial b / \partial x$ (see section 4.2), which can be determined with good accuracy from our high-resolution density observations at position S, we believe that the actual uncertainty in this parameter is significantly smaller. The least known parameter in our computations is the bottom roughness z_0 that is varied in Figure A1c about the reference value $z_0 = 10^{-3}$ m. Doubling or halving z_0 modifies the BBL thickness by less than 10% with respect to the reference simulations, with a tendency for increasing BBL thicknesses if the bottom becomes rougher. We conclude that the uncertainties in our model parameters are unlikely to have a large effect on the modeled BBL thickness that, as shown above, is in good agreement with our data.

While the above parameter variations only have a small to moderate impact on the BBL thicknesses, they do have a large influence on the SPM fluxes, here quantified with the help of the cross-slope transport velocity U_c. For example, a 50% decrease in the standard value for α results in approximately the same reduction in the transport velocity (Figure A1a). A strong sensitivity is also found with respect to the background stratification (Figure A1b), and only variations in the bottom roughness show no significant effect on SPM transport (Figure A1c). Data to evaluate the significance of these variations with respect to U_c are not available.

References

Burchard, H., and R. D. Hetland (2010), Quantifying the contributions of tidal straining and gravitational circulation to residual circulation in periodically stratified tidal estuaries, *J. Phys. Oceanogr.*, *40*, 1243–1262.

Burchard, H., K. Bolding, T. P. Rippeth, A. Stips, J. H. Simpson, and J. Sündermann (2002), Microstructure of turbulence in the northern North Sea: A comparative study of observations and model simulations, *J. Sea Res.*, *47*, 223–238.

Burchard, H., H. Schuttelaars, and A. Geyer (2013), Residual sediment fluxes in weakly-to-periodically stratified estuaries and tidal inlets, *J. Phys. Oceanogr.*, *43*(9), 1841–1861, doi:10.1175/J.Phys.Oceanogr.-D-12-0231.1.

Choi, B. H., K. O. Kim, and H. M. Eum (2002), Digital bathymetric and topographic data for neighboring seas of Korea, *JKSCO*, *14*(1), 41–50.

Emery, W. J., and R. E. Thomson (2001), *Data Analysis Methods in Physical Oceanography*, 2nd ed., 638 pp., Elsevier, Amsterdam.

Endoh, T., Y. Yoshikawa, T. Matsuno, Y. Wakata, K.-J. Lee, and L. Umlauf (2016), Observational evidence for tidal straining over a sloping continental shelf, *CSR*, *117*, 12–19, doi:10.1016/j.csr.2016.01.018.

Garrett, C., P. MacCready, and P. Rhines (1993), Boundary mixing and arrested Ekman layers: Rotating stratified flow near a sloping bottom, *Annu. Rev. Fluid Mech.*, *25*, 291–323, doi:10.1146/annurev.fl.25.010193.001451.

Groen, P. (1967), On the residual transport of suspended matter by an alternating tidal current, *Neth. J. Sea Res.*, *3*(4), 564–574.

Hansen, D. V., and M. Rattray (1965), Gravitational circulation in straits and estuaries, *J. Mar. Res.*, *23*, 104–122.

Hinze, J. O. (1987), *Turbulence*, 2nd ed., 586 pp., McGraw-Hill, New York.

Jay, D. A., and J. D. Musiak (1994), Particle trapping in estuarine tidal flows, *J. Geophys. Res.*, *99*(C10), 20,445–20,461.

Lefevre, F., C. Le Provost, and F. Lyard (2000), How can we improve a global ocean tide model at a regional scale? A test on the Yellow Sea and the East China Sea, *J. Geophys. Res.*, *105*(C4), 8707–8725.

MacCready, P., and W. R. Geyer (2014), The estuarine circulation, *Ann. Rev. Fluid Mech.*, *46*, 175–197, doi:10.1146/annurev-fluid-010313-141302.

Schulz, K., and L. Umlauf (2016), Residual transport of suspended material by tidal straining near sloping topography, *J. Phys. Oceanogr.*, doi:10.1175/JPO-D-15-0218.1, in press.

Scully, M. E., and C. T. Friedrichs (2007), Sediment pumping by tidal asymmetry in a partially mixed estuary, *J. Geophys. Res.*, *112*, C07028, doi:10.1029/2006JC003784.

Simpson, J. H., J. Brown, J. Matthews, and G. Allen (1990), Tidal straining, density currents, and stirring in the control of estuarine stratification, *Estuaries Coasts*, *13*, 125–132.

Simpson, J. H., H. Burchard, N. R. Fisher, and T. P. Rippeth (2002), The semi-diurnal cycle of dissipation in a ROFI: Model-measurement comparisons, *Cont. Shelf Res.*, *22*, 1615–1628.

Umlauf, L., and H. Burchard (2005), Second-order turbulence closure models for geophysical boundary layers. A review of recent work, *Cont. Shelf Res.*, *25*, 795–827.

Umlauf, L., and H. Burchard (2011), Diapycnal transport and mixing efficiency in stratified boundary layers near sloping topography, *J. Phys. Oceanogr.*, *41*(2), 329–345, doi:10.1175/2010JPO4438.1.

Umlauf, L., H. Burchard, and K. Bolding (2005), GOTM—Scientific documentation, version 3.2, *Mar. Sci. Rep. 63*, Leibniz Inst. for Baltic Sea Res., Warnemünde, Germany.

Umlauf, L., W. D. Smyth, and J. N. Moum (2015), The energetics of bottom Ekman layers during buoyancy arrest, *J. Phys. Oceanogr.*, *45*, 3099–3117, doi:10.1175/JPO-D-15-0041.1.

Uncles, R. J., R. C. A. Elliott, and S. A. Weston (1985), Observed fluxes of water, salt and suspended sediment in a partly mixed estuary, *Estuarine Coastal Shelf Sci.*, *20*(2), 147–167.

van Aken, H. M. (1986), The onset of seasonal stratification in shelf seas due to differential advection in the presence of a salinity gradient, *Cont. Shelf Res.*, *5*, 475–485.

Xianwen, B., G. Guoping, and Y. Ju (2001), Three dimensional simulation of tide and tidal current characteristics in the east china sea, *Oceanol. Acta*, *24*(2), 135–149.

Yoshikawa, Y., T. Matsuno, T. Wagawa, T. Hasegawa, K. Nishiuchi, K. Okamura, H. Yoshimura, and Y. Morii (2012), Tidal and low-frequency currents along the CK Line (31deg 45min N) over the East China Sea shelf, *Cont. Shelf Res.*, *50*, 41–53.